

University of Groningen

## Colloidal quantum dot solids

Balázs, Dániel Máté

**IMPORTANT NOTE:** You are advised to consult the publisher's version (publisher's PDF) if you wish to cite from it. Please check the document version below.

*Document Version*

Publisher's PDF, also known as Version of record

*Publication date:*

2018

[Link to publication in University of Groningen/UMCG research database](#)

*Citation for published version (APA):*

Balázs, D. M. (2018). *Colloidal quantum dot solids: Nanoscale control of the electronic properties*. [Thesis fully internal (DIV), University of Groningen]. University of Groningen.

### Copyright

Other than for strictly personal use, it is not permitted to download or to forward/distribute the text or part of it without the consent of the author(s) and/or copyright holder(s), unless the work is under an open content license (like Creative Commons).

The publication may also be distributed here under the terms of Article 25fa of the Dutch Copyright Act, indicated by the "Taverne" license. More information can be found on the University of Groningen website: <https://www.rug.nl/library/open-access/self-archiving-pure/taverne-amendment>.

### Take-down policy

If you believe that this document breaches copyright please contact us providing details, and we will remove access to the work immediately and investigate your claim.

Downloaded from the University of Groningen/UMCG research database (Pure): <http://www.rug.nl/research/portal>. For technical reasons the number of authors shown on this cover page is limited to 10 maximum.

### **3. Counterion-mediated ligand exchange for PbS colloidal quantum dot superlattices**

In the past years halide capping became one of the most promising strategies to passivate the surface of colloidal quantum dots (CQD) in thin films to be used for electronic and optoelectronic device fabrication due to the convenient processing, the strong n-type characteristics and ambient stability of the devices. Here we investigate the effect of three counterions (ammonium, methylammonium and tetrabutylammonium) in iodide salts used for treating CQD thin films, and shed light to the mechanism of the ligand exchange. We obtain two- and three-dimensional square-packed PbS CQD superlattices with epitaxial merging of nearest neighbor CQDs as a direct outcome of the ligand-exchange reaction, and show that the order in the layer can be controlled by the nature of the counterion. Furthermore, we demonstrate that the acidity of the environment plays an important role in the substitution of the carboxylates by iodide ions at the surface of lead-chalcogenide quantum dots. Finally, we show that single-step blade-coating and immersion in a ligand exchange solution such as the one containing methylammonium iodide can be used to fabricate well performing bottom-gate/bottom-contact PbS CQD field effect transistors with record subthreshold swing.

---

This chapter is based on the publication:

D. M. Balazs, D. N. Dirin, H. Fang, L. Protesescu, G. H. ten Brink, B. J. Kooi, M. V. Kovalenko, M. A. Loi, *ACS Nano* 9 (2015) 11951.

### 3.1. Introduction

In 2011, the use of halides during the CQD synthesis was suggested to passivate surface traps.<sup>1,2</sup> Subsequently, these halides were found to replace the original ligands, resulting in n-type CQD solids.<sup>3</sup> This partial halide shell provides a very good passivation of the CQD surface resulting in CQD solids with excellent air stability lacking using the traditional, thiol ligands; the effectiveness of such treatment was demonstrated with the fabrication of highly efficient (8.5%) and ambient-stable solar cells.<sup>4-6</sup> The insertion of heteroatoms onto the surface of the CQDs modifies their electronic structure and can be considered a sort of ‘doping’.<sup>7</sup> Such doping was also exploited to obtain increased thermoelectric effects using hydrochloric acid-treated lead-chalcogenide CQDs.<sup>8</sup> Following these early successes, solution-phase LE to halides, pseudohalides and halometallates have also been accomplished.<sup>9-12</sup>

Even in such relatively simple ligand type as atomic halides, a large range of possibilities is provided by the broad variability of the organic salts and possible solvents. So far, most works have been performed using tetrabutylammonium-iodide (TBAI) dissolved in methanol. However, it has been noticed that using methanol or isopropanol result in different transport properties, but no light was shed to the origin of this difference.<sup>13</sup> However, the non-trivial general role of the solvent in the LE process has also been reported.<sup>14-16</sup> Methanol (compared to other common solvents) has a superior ability to strip the CQD surface from weakly bound ligands, while acetonitrile in the same process is practically inactive.

Here we report about the efficiency of solid-state LE of PbS CQDs with three different iodide salts, namely, ammonium iodide ( $\text{NH}_4\text{I}$ ), methylammonium iodide ( $\text{CH}_3\text{NH}_3^+\text{I}^-$ , MAI), and tetrabutylammonium iodide ( $(\text{C}_4\text{H}_9)_4\text{N}^+\text{I}^-$ , TBAI). The first two have been used so far only in solution-phase LE, with limited success.<sup>12,17</sup> To prove the effectiveness of the LE, in addition to the standard analytical techniques such as infrared absorption and HRTEM, we fabricate field-effect transistors (FETs), and investigate the photoexcitation dynamics of the CQD solids. We reveal the different degree of ordering upon the use of different salts, prove that the counterions play a role in the LE, and show the connection between the reactivity difference and the actual device performance. Furthermore, we demonstrate that the LE is hindered in aprotic conditions, showing that the process is acid-catalyzed, explaining, in this way, the role of the counterions. Importantly, we achieve epitaxial fusion of the CQDs and growth of multilayer superlattices by exposing the as-deposited OA capped CQDs to the LE solutions, and show that the order depends on the reaction conditions. The good superlattice organization obtained with MAI is also evident in the fabricated FETs, which display electron mobility up to  $0.05 \text{ cm}^2/\text{Vs}$ , n-channel on/off ratio up to  $10^6$  and subthreshold swing as low as  $2.4 \text{ V/dec}$ . These findings might ease the fabrication in the near future of cheap and efficient CQD solar cells.

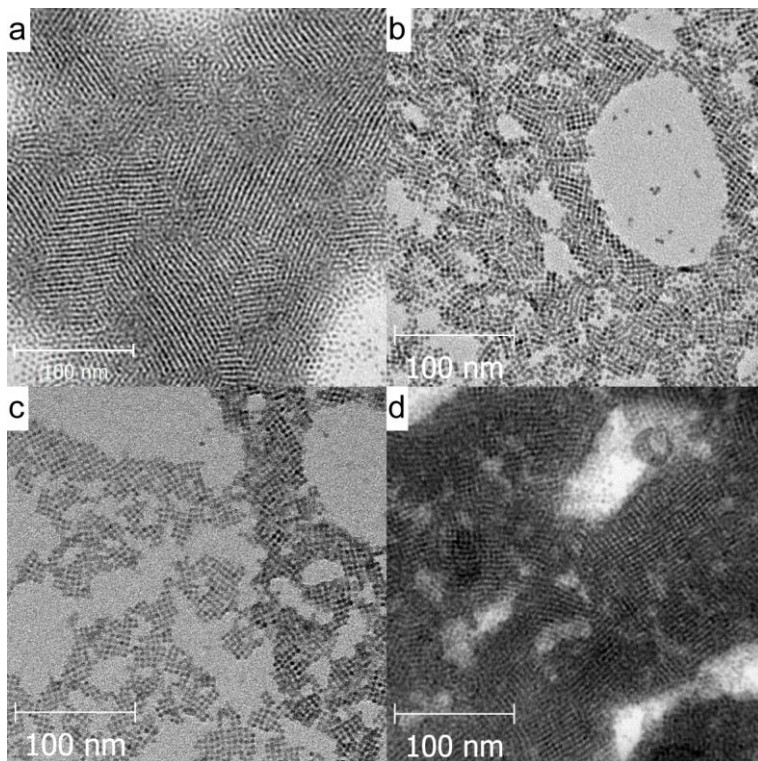


**Figure 3.1** TEM micrographs of (a) as-deposited PbS CQDs and solids formed via exposure to b)  $\text{NH}_4\text{I}$ , c) MAI, and d) TBAI solutions. The original hexagonal symmetry changes to square-like after the treatments, and a different degree of ordering is observable between the samples.

### 3.2. Nanostructure: influence of the counterions and epitaxial fusion

First, the influence of different cations in iodide salts used for the LE on the nanostructure of the layer is investigated. Transmission Electron Microscopy (TEM) images of as-deposited films and ones prepared with the three different salts are reported in Figure 3.1. The oleic acid-capped particles arrange in a hexagonal close-packed fashion, as can be seen in Fig. 3.1(a). A square-lattice arrangement is observable on panels (b-d), which is clearly induced during the LE process. Interestingly, the domain size appears to depend on the applied counterion in the LE process. Domains of only a few CQDs and a single layer are observed for the sample fabricated with  $\text{NH}_4\text{I}$  (Fig. 3.1(b)), extended lattices and simultaneous formation of double layers are found in MAI (Fig. 3.1(c), see the darker areas on the right side of the image); even larger domains and multiple layers are present in the case of TBAI-treated samples (Fig. 3.1(d)).

A High Resolution Transmission Electron Microscopy (HRTEM) image of the QDs assembled with MAI, and its 2D Fourier-transformation (FT) are displayed in Figure 3.2(a) and 1(b), respectively. The real-space image shows that the CQDs are oriented in the same crystallographic direction. The combination of two patterns is observed on the FT image; in addition to the broad first- and second-order pattern of the rock-salt PbS structure, the smaller features related to the larger spacing of the superlattice are also visible around the zero order (since the unit vectors of the superlattice are roughly 15 times longer than the PbS lattice vectors). The profile extracted from the FT image is shown on panel (c), demonstrating that the directions of the two diffraction patterns coincide, and that the primitive vectors of the superlattice lie in the  $\langle 100 \rangle$  directions of the PbS rock-salt lattice (see also Fig. 3.2(d)). Analogous self-organization along  $\langle 100 \rangle$  axes has been observed earlier for square<sup>18-22</sup> and honeycomb<sup>23</sup> PbSe CQD superlattices. Both PbS and PbSe CQDs are usually approximated as truncated octahedron or rhombicuboctahedron with 3 types of facets: {100}, {110} and {111} (Fig. 3.2(e)). Among those, {100} is the least acidic with Pb coordination number 5 whereas Pb atoms on {110} and {111} facets have coordination numbers 4 and 3, respectively. This should lead to a higher affinity of anionic ligand species to the latter facets leaving {100} facets more opened. Zhrebetskyy *et al.*, calculated that un-passivated {100} facets of PbS CQDs have approximately 2 times lower surface energy than the {111} facets and ligands can be easily removed from the {100} surface.<sup>24</sup> These facts together explain the observed self-organization of lead chalcogenide CQDs along  $\langle 100 \rangle$  axes upon the exchange of bulky organic ligands with small inorganic anions.

Furthermore, the honeycomb PbSe superlattices reported in ref. 23 fit these observation as well, since they can be considered as formed by the same primitive cubic superlattice viewed from the  $\langle 111 \rangle$  direction. This orientation is formed and stabilized by the affinity difference of the OA to the different facets, and the preferred exposure of the {111} facets to the surrounding medium due to the higher OA-coverage. In our case, the reactive *in situ* LE to small anions allows minimum amount of bulky organic leftovers, and the substrate used in these experiments has no preference towards the capped facets, leading to a denser structure, where the  $\langle 100 \rangle$  axis perpendicular to the surface. Similarly, drying of colloidal solutions of PbS QDs with undetectable amount of bulky organic ligands (prepared by solution-phase LE to  $\text{PbI}_3^-$  anions, with  $\text{MA}^+$  as counterion)<sup>10</sup> also form square superlattices with CQD orientation along  $\langle 100 \rangle$  axes (Fig. 3.3).

The higher resolution image in Fig. 3.2(d) reveals that the CQDs' crystal lattice is continuous at the necking points, in other words the CQDs are epitaxially fused together along the {100} facets. The superlattice spacing is found to be about 4.5 nm for iodide-capped CQDs of 3.8 nm size, and does not depend on the cation employed, in case of ordered domains. The increase of bond length in CQD superlattices with face-to-face attachment was observed and discussed also in ref. 23 and 25; briefly, after atomic orientation of the CQDs, a gradual removal of remaining ligands occurs, which is followed by diffusion of Pb and S atoms into the interdot gap. Obviously, the inter-particle distance right before necking depends on the original ligand size. This explains why the observed

bond lengths (neck stretching) are constant for all iodide-capped CQDs, and gives a convenient tool for further controlling the nanostructure of the layer.

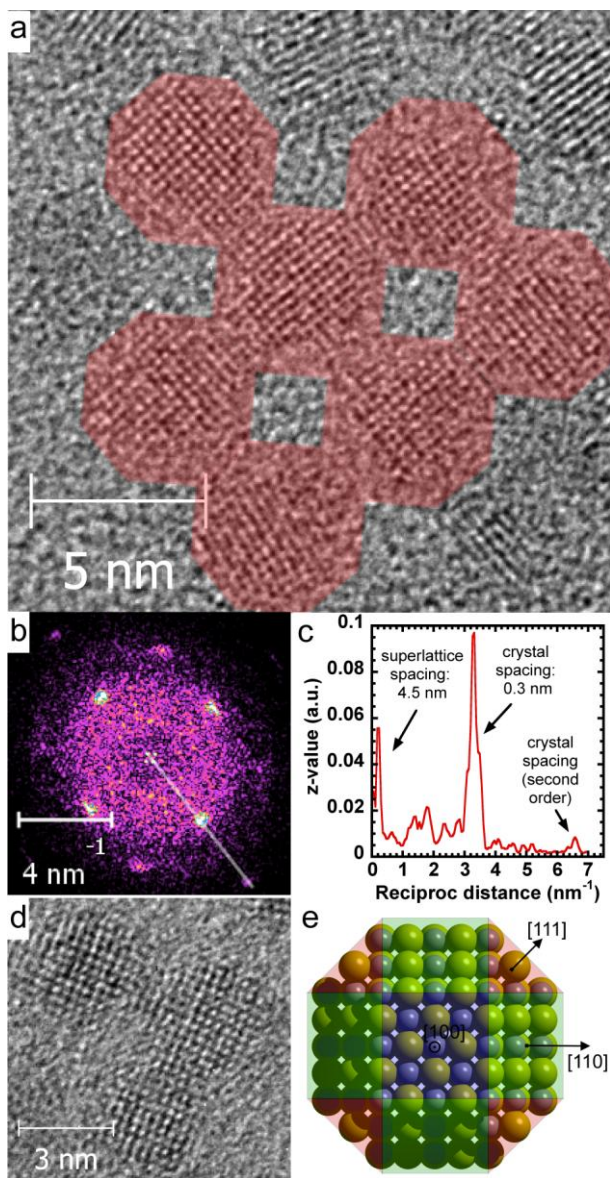


**Figure 3.2** (a) Real-space and (b) Fourier-transformed HRTEM images, and (c) an extracted line profile from the FT image of a domain showing that the superlattice consists of CQDs oriented the same direction after treatment; (d) high resolution image on the oriented assembly showing epitaxially connected CQDs; (e) schematic structure with the main facets of a PbS CQD.

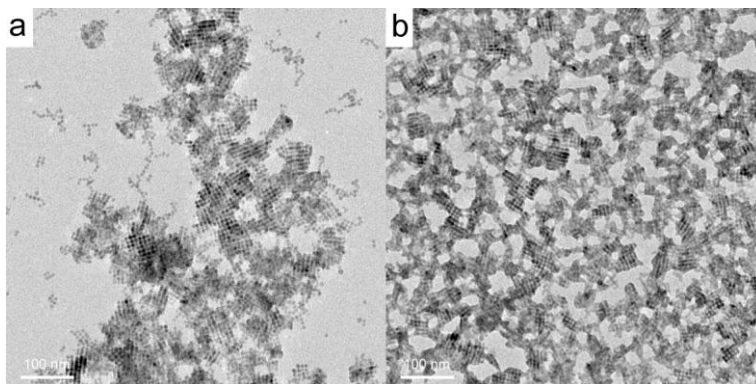


**Figure 3.3** TEM images of MAPbI<sub>3</sub>-capped PbS QDs deposited (a) from pure PC and (b) with MFA additive showing the different degree of organization.

As mentioned above, the QDs appear to have reoriented during the LE process in order to interact between each other with the same facets, minimizing in this way the overall surface area, analogously to the “oriented attachment” occurring in solution.<sup>25</sup> This implies that the self-orientation of the single QDs induces a macroscopic orientation at the superlattice-level. The orientation is so powerful that it occurs even during a rapid LE employed in this research. It is important to notice that this assembly occurs in three dimensions, as seen from the multilayer structures on Fig. 3.1(c-d), opening up exciting possibilities in designing new QD-based metamaterials.

### 3.3. Optical properties

Absorbance, steady-state and time-resolved photoluminescence of the three samples prepared with different iodide salts were recorded to understand if the observed differences in the nanostructures affect the electronic configuration and therefore the photophysical properties. Figure 3.4(a) reports the absorption spectra displaying a well-pronounced excitonic peak for all three samples and identical peak position (1070 nm). The photoluminescence spectra of the different samples in Figure 3.4(b) are also practically identical with peaks around 1240 nm. Furthermore, the time resolved measurements (Figure 3.4(c)) performed on the samples in inert atmosphere also display very similar lifetimes. The same peak position of the absorption and the photoluminescence spectra and the similar excitation lifetimes suggest that the samples are electronically identical (the emission originates from the same state) and that the degree of electronic wavefunction delocalization, thus the average electronic coupling is also identical.

Recently, a dependence of the PL lifetime on the TBAI concentration was reported by Bawendi *et al.* for PbS QDs.<sup>26</sup> For concentrations similar to what is used in this work, much slower decay was observed. Besides their instrument having a worse time resolution, the higher coupling achieved here through longer exposure to the LE solution and more careful washing may be the origin of the difference.

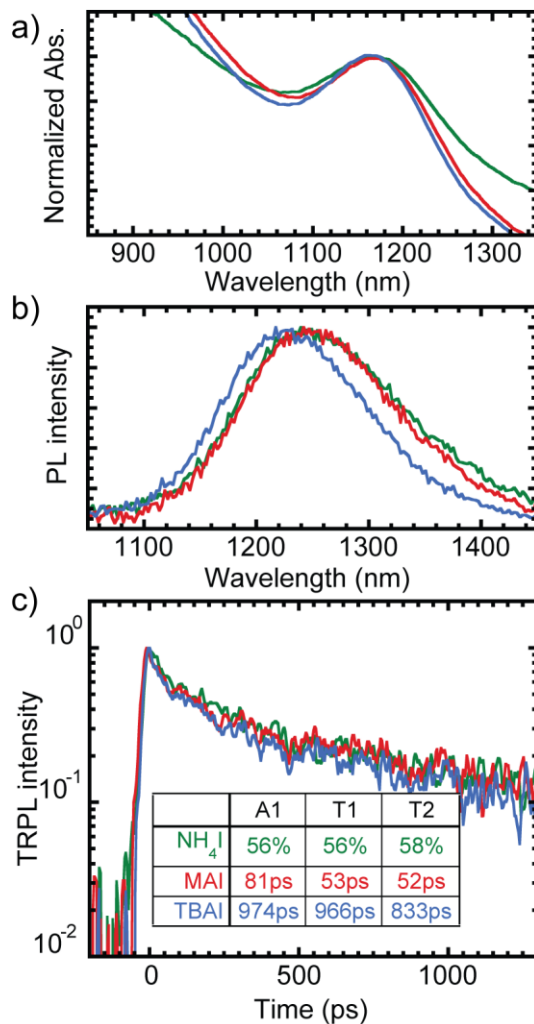


**Figure 3.4.** Optical spectroscopy data of thin films prepared with the three salts: a) absorbance b) steady-state and c) time-resolved photoluminescence. The data indicate no difference in the electronic coupling.



### 3.4. Transport properties determined by the ligand exchange conditions

For the prospective applications, we sought to shed light onto the influence of the counterions on the charge transport properties. Field-effect transistors (FETs) are exceptionally sensitive to the material's quality; therefore they can be used as a general testing method, although one has to consider numerous factors that influence the measured current. We fabricated FETs of PbS CQDs using blade-coating, which is known to be an efficient and scalable method for the preparation of solution-based thin films. This one-step deposition allows simplifying the fabrication of CQDs transistors, going away from the material-costly spin-coating method and from the time-consuming layer-by-layer approach.<sup>27,28</sup> Details of the fabrication are reported in the experimental section; briefly, we deposit the desired thickness on a pre-patterned Si/SiO<sub>2</sub> substrate, which also acts as the gate electrode, the CQD layer is then dipped into the LE solution.

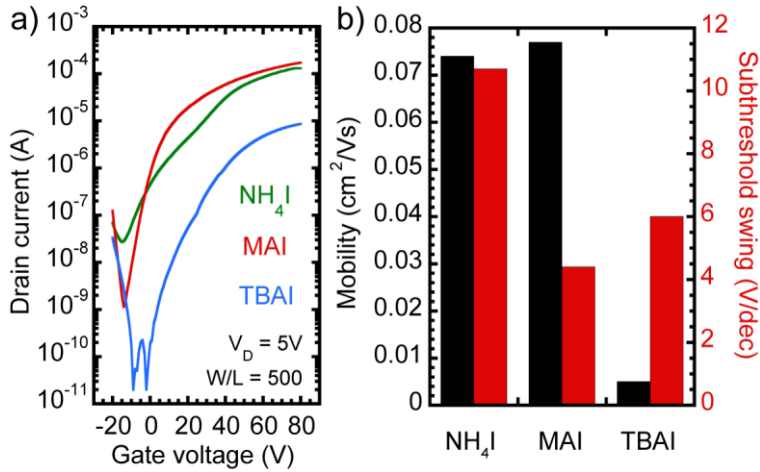


**Figure 3.5** (a)  $I_D$ - $V_G$  curves of PbS CQD FETs fabricated using different LE solutions; (b) extracted linear regime electron mobility and n-channel subthreshold swing values for the different ligands.

Figure 3.5(a) shows the transfer curves of FETs fabricated with 30 nm PbS films treated with the three different solutions. We compare the subthreshold and the linear current regime behavior using the extracted subthreshold swing and mobility values in Figure 3.5(b). All transfer curves show similar main characteristics, electron-dominated weak ambipolarity, with a substantially different quality of the transport for the different ligands. In contrast to the CQD organization trend observed on the TEM images, the maximum currents show a  $\text{TBAI} < \text{NH}_4\text{I} \approx \text{MAI}$  trend, which is confirmed by the extracted mobility values. The subthreshold swing was found to be the lowest for the FET prepared using MAI, and was the highest for the one with  $\text{NH}_4\text{I}$ . There is only a marginal difference

between the ‘on’ state behaviors of the  $\text{NH}_4\text{I}$ - and MAI-treated samples, but their ‘off’ currents are considerably different. The FET prepared with TBAI showed instrument-limited ‘off’ current, likely hiding the real subthreshold region, which might be due to the overall lower conductivity. One and three order of magnitude higher ‘off’ currents were measured in the MAI and  $\text{NH}_4\text{I}$  samples, respectively; the increase may be explained with the generation (or left-over) of charged species in the band gap during the LE.

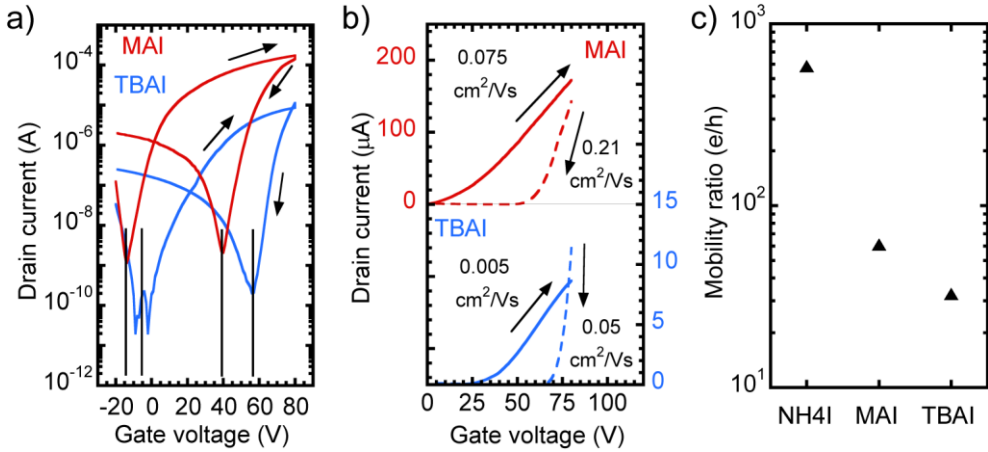


**Figure 3.6** Hysteresis of the (a) off-state voltage and (b) mobility in FETs prepared with MAI and TBAI reactants, and (c) ratio of electron and hole mobilities.

The subthreshold swing is a direct measure of the sub-bandgap trap density in the thin film and at its interface with the dielectric.<sup>29</sup> Since the  $\text{SiO}_2$  surface is the same in all fabricated devices, the bulk properties of the films account for the difference in the swing. The higher swing (lower logarithmic slope in the subthreshold region) means higher trap density, or in other words, more states to be filled before the Fermi-level reaches the conduction band. Based on the TEM results (Fig. 3.1), the increased energy disorder due to positional disorder may also account for the different trap density, resulting in a wider and deeper distribution of energy levels. However, the significance of this influence is minimal, since the transport in disordered systems generally occurs through states below the conduction band (above the valence band), leading to an apparent shallower band tail.<sup>30</sup> Comparing the hysteresis of the MAI- and TBAI-treated samples (Fig. 3.6), it is clear that the subthreshold behavior is similar in the forward and reverse scans for both samples (ruling out large difference in the sub-bandgap energy distribution and significant filling of these states). However, the difference between the forward and reverse slopes is significant, which correlates with filling the trap states below the transport edge, causing a mobility increase.<sup>31</sup> This shift is higher in the TBAI-based FET (showing 10-fold mobility increase compared to the 2.7-fold in the MAI-based FET); this fact together with the minimal difference in the sub-bandgap trap density suggest the presence of deep trap states. A difference in the doping levels may also explain the overall higher conductivity achieved

with MAI treatment compared to the TBAI one. However, a change in the dopant concentration is expected to shift the ratio of the hole and electron mobilities, which balance is roughly the same for TBAI and MAI. Consequently, the low conductivity of the TBAI sample seems to be related to a higher amount of traps. In the case of  $\text{NH}_4\text{I}$  the electron/hole balance changes significantly respect to the other two ligands, see and the mobility ratios on Fig. 3.6(c), indicating a probable extrinsic doping (leftover of charge species) which is also in agreement with the higher off current.

FTIR spectra of the films were taken (Figure 3.7) to check the completeness of the LE. The peaks around 2900 and 1400-1600  $\text{cm}^{-1}$  are signatures of the remaining oleic acid after LE for the same 1 min exposure time; significant presence of ammonium ions can be ruled out since the NH or CN signatures are missing. Remains of OA are seen in the  $\text{NH}_4\text{I}$ -, and in increased amount in the TBAI-treated samples, suggesting incomplete LE, while no traces of oleic acid can be detected in samples prepared using with MAI.

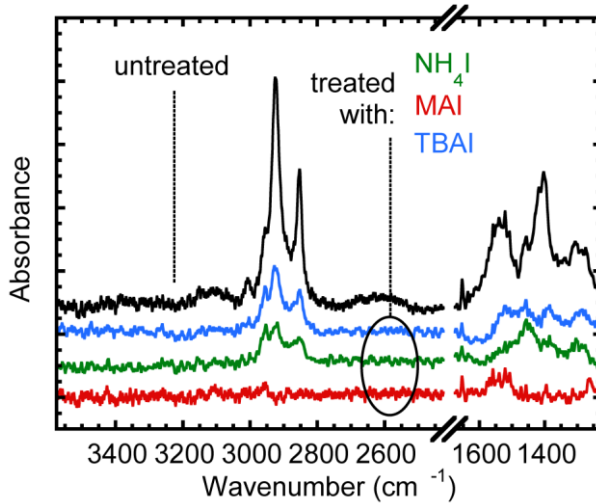


**Figure 3.7.** (c) FTIR spectra of the different samples showing varying amount of oleic acid.

Altogether these findings suggest that MAI is superior to both  $\text{NH}_4\text{I}$  and TBAI for the fabrication of well performing CQD FETs. Therefore the deposition process was further optimized for high mobility and low subthreshold swing. In Figure 3.8 are reported the output and transfer characteristics of the best device. A n-channel on/off ratio around  $10^6$  and subthreshold swing as low as 2.4 V/dec are the most relevant features. The latter is the lowest value reported for CQD transistors using  $\text{SiO}_2$  gating. In these samples, the electron mobility is around  $0.5 \text{ cm}^2/\text{Vs}$ , while the hole mobility is much lower ( $3 \times 10^{-5} \text{ cm}^2/\text{Vs}$ ).

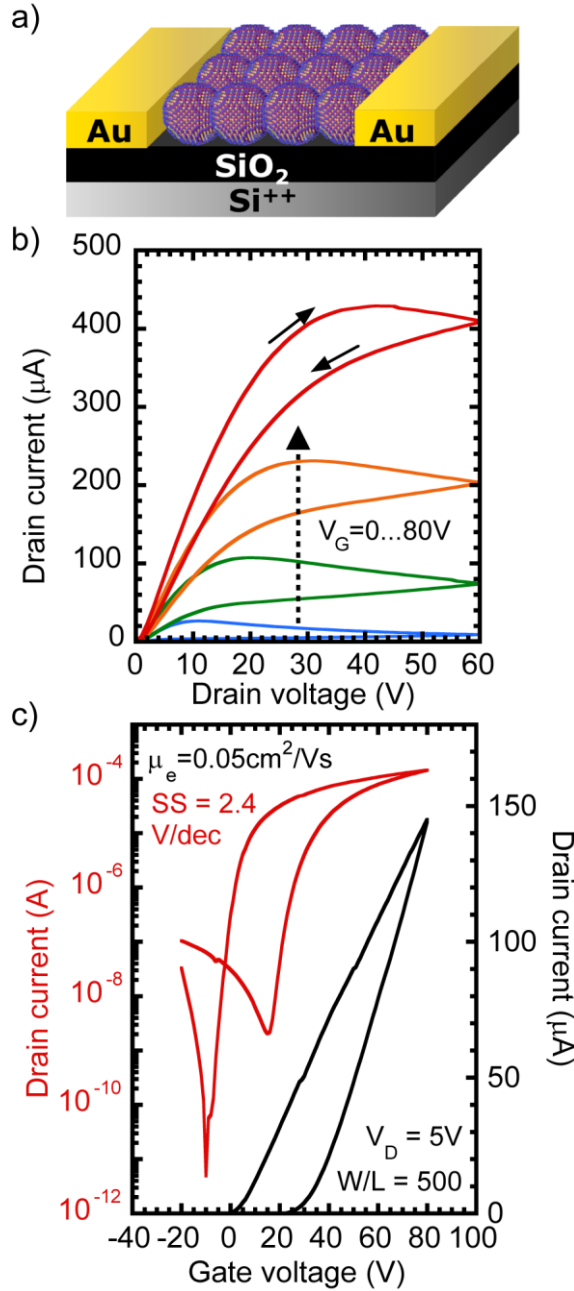


**Figure 3.8** (a) Schematic device structure of the PbS CQD FETs (b)  $I_D$ - $V_D$  (output) and (c)  $I_D$ - $V_G$  (transfer) characteristics measured in one of the champion MAI-treated devices. The average mobility is  $0.043 \pm 0.011 \text{ cm}^2/\text{Vs}$  and the average subthreshold swing is  $4.0 \pm 0.9 \text{ V/dec}$  calculated on 95% confidence from 14 samples.

### 3.5. Catalytic mechanism of the ligand exchange process

As observed already with the TEM reported in Fig. 3.1, treatments of the same duration result in films with different disorder depending on the counterion used. Also, partial delamination and cracking of the films is observed frequently using  $\text{NH}_4\text{I}$ , and only very occasionally using MAI. These phenomena seems to suggest that the LE for  $\text{NH}_4\text{I}$  is too fast to leave sufficient time for a full reorganization of the CQDs; at the same time, the LE using TBAI appears to be mild, but incomplete, resulting in many defect states and large oleic acid leftover. These observations could indicate a reactivity difference between the three salts; we therefore investigated if the LE is acid catalyzed and if the acidity of the cations influences the exchange rate.

To test this hypothesis, we performed experiments where no protic species are present (namely TBAI, the non-protic salt was dissolved in aprotic acetonitrile). By measuring the transistor fabricated in this way, we found that the LE does not take place in fully aprotic conditions, even up to 10 minutes exposure, as shown on Figure 3.9(a). Large amount of oleic acid was found in the film (see the bound  $\text{COO}^-$  peak at around  $1530\text{ cm}^{-1}$  and the CH stretching peaks around  $2900\text{ cm}^{-1}$  (Figure 3.9(b)), and the film remained soluble in apolar solvents. We observed the same inactivity using other polar aprotic solvents, such as propylene carbonate and  $\gamma$ -butyrolactone (Fig. 3.10). However, upon addition of formic acid to the acetonitrile solution, the LE takes place as in methanol, and the film turns conductive; the conductivity in both n- and p-channels depends on the acid concentration (see Fig. 3.9(a)). Importantly, the sign of the charge carriers in these experiments is significantly different from that of the formic acid-only treatment, which suggests that the CQDs are not capped by formate instead of iodide, but the former assists the attachment of the latter. Proof for the removal of the oleic acid and the absence of bound formate species is obtained by FTIR measurements showing no signs of either CH or bound  $\text{COO}^-$  peaks (Fig. 3.9(b)).

The fast oleic acid–formic acid replacement is driven by the higher adsorption energy of the shorter aliphatic ligand in polar solvent, since the functional groups are the same.<sup>32</sup> Energetically, the same stands for the oleate–iodide couple (given the high lattice energy of lead-iodide), but the lack of acidic species in the mixture seems to hinder the reaction. Based on this difference, we suggest that the presence of acidic species in the solution can stabilize ligand removal analogously to the equilibrium ligand stripping achieved in ref. 22. The surface is then partially “naked”, and the equilibrium will be shifted towards capping with the strongest binding ligand present in the solution, in the order: oleate<formate<iodide. Whether the stabilization is of protic or Lewis-acidic origin, remains a topic of future investigations.

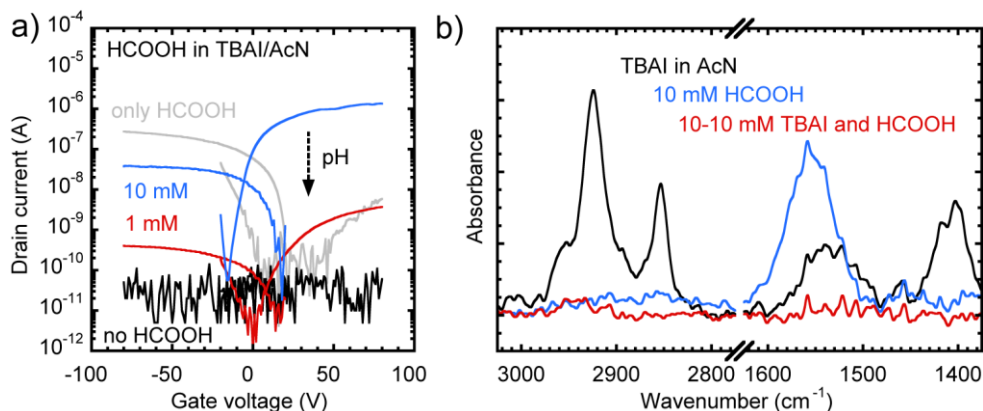


**Figure 3.9** (a)  $I_D$ - $V_G$  (transfer) curves of FETs fabricated using acetonitrile solutions containing 10 mM TBAI and 0 mM, 1 mM or 10 mM HCOOH; (b) the corresponding FTIR spectra showing the removal of oleic acid and the lack of carboxylate groups in the iodide-treated sample in presence of acid.

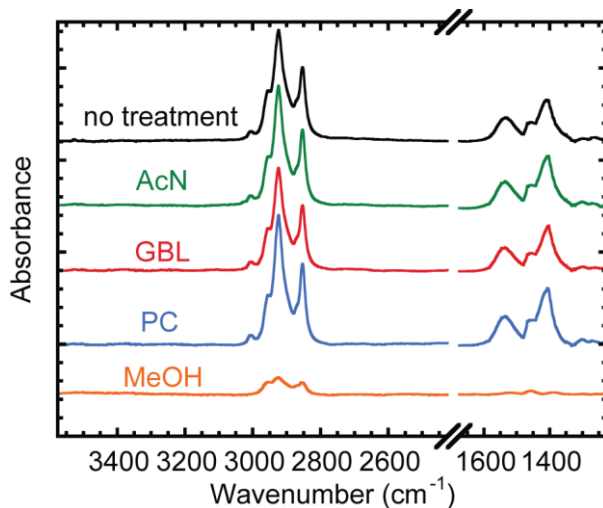


**Figure 3.10.** FTIR spectra of PbS-OA thin films after treatment with TBAI in different solvents (AcN: acetonitrile, PC: propylene carbonate, GBL:  $\gamma$ -butyrolactone). The absorbance peaks show very similar OA content.

Furthermore, we found that LE occurs when the PbS CQD film is exposed to MAI dissolved in acetonitrile, likely through the mediation of the acidic counterion. If the reaction is indeed happening through the contribution of acidic species, addition of a base (with low affinity to the surface) will decrease the LE reaction rate. To demonstrate the deactivation of the LE solution, we added different concentrations of triethylamine (TEA)

in an acetonitrile solution of MAI. With this, we expect that the acidity of the  $\text{MA}^+$  will be masked by its interaction with the strongest base present, the TEA. We found that films treated at higher pH show lower conductivity after the same exposure time (Figure 3.11(a)), and the amount of oleic acid remaining in the film increases accordingly (Figure 3.11(b)). The simultaneous variation of the p-channel and n-channel currents in the transistor suggests increasing resistance in the layer, and not doping or trapping effects, which would influence only one of the channels. Moreover, the  $\text{CH}_2$  and  $\text{CH}_3$  peak ratios, the similar trend in the  $\text{COO}^-$  peak and the lack of CN vibration also rule out TEA being adsorbed on the surface; therefore the incomplete exchange of the OA is the cause of the lower current.

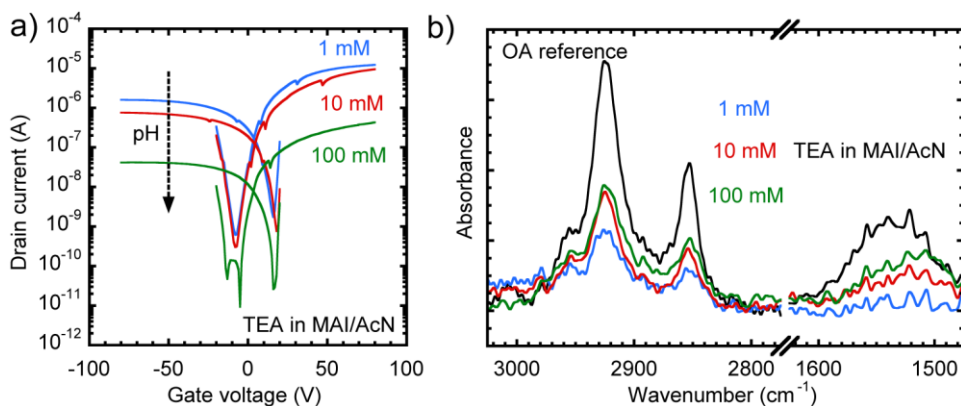


**Figure 3.11.** a)  $I_D$ - $V_G$  (transfer) curves measured in layers treated with acetonitrile solutions containing 10 mM MAI and 1 mM, 10 mM or 100 mM TEA; b) the corresponding FTIR spectra showing different amount of remaining oleic acid at different pH.

The same consideration about the pH effect on ligand removal is relevant not only for the original organic ligands, but also for the new inorganic anionic species (*e.g.*  $\text{PbI}_3^-$ ). Since ligand removal can be promoted/hindered by the presence/absence of acidic species, one can control the rate of the CQDs' "oriented attachment" by solvent acidity. In order to prove it, we used two solutions of  $\text{MAPbI}_3$ -capped PbS CQDs: the first, in net aprotic protophobic propylene carbonate (PC), and the second in PC with addition of N-methylformamide (MFA:PC=1:100), which is a strong H-bond donor solvent (one of the strongest among the non-alcohols). We observed the previously described square-ordered superlattices in both cases, but the level of ordering was noticeably different (Fig. 3.3(a-b)). The sample deposited from pure PC demonstrated relatively low level of ordering, whereas the MFA additive allowed notable extension of the ordered domains of QDs. In this case, the non-acidic PC does not provide a driving force for the ligand removal in solution, thus only a low number of CQDs have ligand-free, reactive facets that can participate in the "oriented attachment". On the other hand,  $\text{PbI}_3^-$  ions are stabilized in solution in the presence of MFA,<sup>10</sup> increasing the number of "naked" CQDs, which is a prerequisite for the "oriented attachment" and the formation of large domains.

Clearly, the reactivity of the environment affects the CQDs ordering during *in situ* LE, as well as the transport in the layer. The use of TBAI, where only the weak acid solvent catalyzes the LE, leads to extended superlattice domains, since more time is available for the “oriented attachment”. However, when considering the electronic properties, the lower reactivity is less attractive, since low conductivity and worse material quality (in sense of high trap density) are achieved. The lower acidity of isopropanol than methanol can also account for the increased trap density reported in the literature.<sup>13</sup> Longer (*e.g.* 10 minute) exposure to the TBAI-methanol solution leads to improvement in the transport, but the mobility is still below that of in the MAI sample. This suggests that there may be other factors causing the dissimilar conductivity, such as the  $\text{TBA}^+$  ions being unable to diffuse fast through the layer. If the solubilized oleates are not replaced by iodide ions due to diffusion problems, the unbalanced surface chemistry will likely cause charge trapping. Consequently, if one aims for one-step deposition of thicker layers (*e.g.* hundreds of nanometers for a solar cell) at a reasonable timescale, TBAI has to be dropped and a different salt has to be chosen.

The acidic ammonium and methylammonium cations increase the reactivity of the LE solution, leading to higher disorder, with FET mobilities invariant with the exposure time within the measurement reproducibility limits. However, the ‘off’ current is very high in the  $\text{NH}_4\text{I}$ -treated sample, which is either result of the presence of mobile ionic species, or stems from the increased n-type doping. As we have demonstrated here a fine tuning of the reactivity of the ligands may be obtain by tuning the acidity of the solution.

### 3.6. Conclusions

To conclude, we showed that epitaxial growth of extended CQD superlattices can be obtained simply by immersing a PbS CQD film into a solution of an iodine salt, and that these ordered regions extend in 3D leading to largely improved FETs subthreshold behavior. We found that TBAI dissolved in methanol shows low reactivity, not providing complete LE in a short time, while both MAI and  $\text{NH}_4\text{I}$  are capable thereof. We delivered proof for an acidic catalysis mechanism of the exchange of carboxylates on the surface of lead-chalcogenides to iodide ions, likely through improved organic ligand displacement. Furthermore, the higher reactivity of  $\text{NH}_4\text{I}$  compared to MAI is due to the higher acidity of the cation which is responsible for a higher disorder and worse carrier transport in the layers. Finally, we showed that single-step blade-coating and immersion in a LE solution can be used to fabricate well performing bottom-gate/bottom-contact PbS CQD field effect transistors.



### 3.7. Experimental methods

**Materials:** The reagents and solvents mentioned below were used as received. Methylammonium iodide was prepared following a literature recipe.<sup>33</sup> Briefly, 24 mL methylamine (33% in ethanol) and 10 mL HI (57% in water) are mixed in 100 mL ethanol at 0°C with constant stirring for 2 h. The salt is formed upon evaporation of the solvent at 60 °C on a hotplate, and the product is washed three times with ethyl ether and dried in vacuum at 60 °C overnight. PbS quantum dots of 3.8 nm diameter capped with oleic acid and dispersed in chloroform were synthesized as reported previously, using a hot-injection method.<sup>34</sup> A lead precursor solution consisting of 1.516 g  $\text{PbAc}_2 \cdot \text{H}_2\text{O}$  in 50 mL ODE and 4.5 mL OA is vacuum dried at 120 °C in a three-neck reaction flask. The temperature is subsequently raised to 145 °C after which a sulfur precursor of 0.420 mL  $\text{TMS}_2\text{S}$  in 10 mL ODE is quickly injected and the flask cooled in a water bath. Toluene and ethanol are added to the solution, followed by centrifugation to separate the QDs. Two more washing steps are performed by re-dispersion in toluene and precipitation by ethanol, and then the particles are dried. Re-dispersion in anhydrous chloroform and precipitation with methanol results in the desired cleanliness, followed by re-dispersion in anhydrous chloroform. Anhydrous solvents were also used for the fabrication of samples for spectroscopy and transistors.

PbS CQDs for LE with  $\text{MAPbI}_3$  were prepared in the same way except that 30 mL ODE and 20 mL OA was used, whereas injection was carried out at 120°C. After washing CQDs were redissolved in hexane. LE was performed according to the literature recipe.<sup>10</sup> 1.5 mmol of MAI and 1.5 mmol of  $\text{PbI}_2$  were dissolved in 30 mL MFA. Solution of organically-capped PbS CQDs in hexane (150 mg/30 mL) was added to ligand solution. The biphasic system was stirred vigorously for 12 hours, until the CQDs are completely transferred from nonpolar to polar organic phase. The hexane layer was removed and the MFA solution was rinsed 3 times with pure hexane. To remove the excess of metal halide ligands, the particles were precipitated from MFA by acetone, centrifuged and redispersed in 1.5 mL MFA.

**TEM characterization:** TEM micrographs were taken using a FEI Tecnai G2, a JEOL JEM-2010 or a Hitachi HD2700CS (STEM) instrument; Fourier-transform images were calculated from selected areas of the micrographs. OA-capped PbS CQDs were deposited onto carbon grids by drop-casting from a dilute solution, followed by immersion in the LE solution and solvent. The MFA solution was diluted 100 times by propylene carbonate, and the samples were dried at 80°C in vacuum. For PC solution of CQDs, we additionally precipitated  $\text{MAPbI}_3$ -capped particles from MFA by toluene and re-dissolved in pure PC. Samples from PC have been dried on TEM grids at 85°C in vacuum.

**FET fabrication:** For device fabrication, oleic acid-capped quantum dots were deposited by blade-coating on HMDS-treated Si/SiO<sub>2</sub> wafers with pre-patterned gold electrodes.<sup>35</sup> The optimal parameters for the deposition were found to be 10 mg/mL CQD concentration, 25 mm/s blade speed and 30°C substrate temperature, resulting in 20-22 nm thickness. The films were immersed in a 10 mM solution of the ligand in methanol (or acetonitrile) for 1 minute, and then washed with clean solvent for another minute. The reaction time was

measured precisely to get comparable results. These parameters were used for all the devices, unless it is specifically mentioned. The fabrication was finished by baking the samples at 120°C for 20 minutes, which does not sinter the CQDs. All steps took place in a glovebox, as well as the transport measurements. For this, an Agilent E5262A semiconductor parameter analyzer was used. The mobility values were calculated from the linear regime transfer curves, from the forward scan ( $|V_D|$  increases in time) to avoid the screening effect of trapped carriers.<sup>36</sup> Similar behavior observed in >10 devices confirmed the reproducibility.

FTIR measurements were performed on films deposited on double-polished silicon wafers following the protocol used for FET fabrication. The measurements were done using a Bruker IFS 66/v in transmission mode or with a Shimadzu IRTracer100-ATR averaging 50 scans.

Photoluminescence spectroscopy: Photoluminescence measurements were performed on samples prepared on quartz substrates by 4 times repeating the deposition to achieve ~90 nm thickness. The second harmonic (400 nm) of a Ti:sapphire laser (Coherent, Mira 900, repetition rate 76 MHz) was used to excite the samples. The optical emission was spectrally dispersed in a single spectrometer and recorded by a cooled array-detector (Andor, iDus 1.7  $\mu\text{m}$ ). Time-resolved PL spectra were detected using a Hamamatsu streak camera with a cathode sensitive to near-IR radiation. The excitation density was reduced to 7  $\mu\text{J}/\text{cm}^2$  by a neutral density filter and the samples were encapsulated to prevent photodegradation during the experiment. All PL transients were fitted with bi-exponential functions.

### 3.8. References

- [1] J. Tang, K. W. Kemp, S. Hoogland, K. S. Jeong, H. Liu, L. Levina, M. Furukawa, X. Wang, R. Debnath, D. Cha, K. W. Chou, A. Fischer, A. Amassian, J. B. Asbury, E. H. Sargent, *Nature Materials* 10 (2011) 765.
- [2] J. Zhang, J. Gao, E. M. Miller, J. M. Luther, M. C. Beard, *ACS Nano* 8 (2014) 614.
- [3] D. Zhitomirsky, M. Furukawa, J. Tang, P. Stadler, S. Hoogland, O. Voznyy, H. Liu, E. H. Sargent, *Advanced Materials* 24 (2012) 6181.
- [4] C. H. Chuang, P. R. Brown, V. Bulovic, M. G. Bawendi, *Nature Materials* 13 (2014) 796.
- [5] P. Stadler, S. A. Mohamed, J. Gasiorowski, M. Sytnyk, S. Yakunin, M. C. Scharber, C. Enengl, S. Enengl, D. A. M. Egbe, M. K. El-Mansy, S. S. A. Obayya, N. S. Sariciftci, K. Hingerl, W. Heiss, *Advanced Materials* 27 (2015) 1533.
- [6] R. W. Crisp, D. M. Kroupa, A. R. Marshall, E. M. Miller, J. Zhang, M. C. Beard, J. M. Luther, *Scientific Reports* 5 (2015) 9945.
- [7] O. Voznyy, D. Zhitomirsky, P. Stadler, Z. Ning, S. Hoogland, E. H. Sargent, *ACS Nano* 6 (2012) 8448.
- [8] M. Ibáñez, R. J. Korkosz, Z. Luo, P. Riba, D. Cadavid, S. Ortega, A. Cabot, M. G. Kanatzidis, *Journal of the American Chemical Society* 137 (2015) 4046.
- [9] A. T. Fafarman, W. K. Koh, B. T. Diroll, D. K. Kim, D. K. Ko, S. J. Oh, X. Ye, V. Doan-Nguyen, M. R. Crump, D. C. Reifsnyder, C. B. Murray, C. R. Kagan, *Journal of the American Chemical Society* 133 (2011) 15753.
- [10] D. N. Dirin, S. Dreyfuss, M. I. Bodnarchuk, G. Nedelcu, P. Papagiorgis, G. Itskos, M. V. Kovalenko, *Journal of the American Chemical Society* 136 (2014) 6550.
- [11] H. Zhang, J. Jang, W. Liu, D. V. Talapin, *ACS Nano* 8 (2014) 7359.
- [12] Z. Ning, H. Dong, Q. Zhang, O. Voznyy, E. H. Sargent, *ACS Nano* 8 (2014) 10321.
- [13] P. Stadler, B. R. Sutherland, Y. Ren, Z. Ning, A. Simchi, S. M. Thon, S. Hoogland, E. H. Sargent, *ACS Nano* 7 (2013) 5757.
- [14] M. Law, J. M. Luther, O. Song, B. K. Hughes, C. L. Perkins, A. J. Nozik, *Journal of the American Chemical Society* 130 (2008) 5974.
- [15] A. Hassinen, I. Moreels, K. De Nolf, P. F. Smet, J. C. Martins, Z. Hens, *Journal of the American Chemical Society* 134 (2012) 20705.
- [16] A. R. Kirmani, G. H. Carey, M. Abdelsamie, B. Yan, D. Cha, L. R. Rollny, X. Cui, E. H. Sargent, A. Amassian, *Advanced Materials* 26 (2014) 4717.
- [17] S. Kim, J. Noh, H. Choi, H. Ha, J. H. Song, H. C. Shim, J. Jang, M. C. Beard, S. Jeong, *The Journal of Physical Chemistry Letters* 5 (2014) 4002.

- [18] W. K. Koh, S. R. Saudari, A. T. Fafarman, C. R. Kagan, C. B. Murray, *Nano Letters* 11 (2011) 4764.
- [19] W. J. Baumgardner, K. Whitham, T. Hanrath, *Nano Letters* 13 (2013) 3225.
- [20] S. J. Oh, Z. Wang, N. E. Berry, J. H. Choi, T. Zhao, E. A. Gaulding, T. Paik, Y. Lai, C. B. Murray, C. R. Kagan, *Nano Letters* 14 (2014) 6210.
- [21] S. J. Oh, N. E. Berry, J. H. Choi, E. A. Gaulding, H. Lin, T. Paik, B. T. Diroll, S. Muramoto, C. B. Murray, C. R. Kagan, *Nano Letters* 14 (2014) 1559.
- [22] S. E. Doris, J. J. Lynch, C. Li, A. W. Wills, J. J. Urban, B. A. Helms, *Journal of the American Chemical Society* 136 (2014) 15702.
- [23] M. P. Boneschanscher, W. H. Evers, J. J. Geuchies, T. Altantzis, B. Goris, F. T. Rabouw, S. A. van Rossum, van der Zant, H S, L. D. Siebbeles, G. Van Tendeloo, I. Swart, J. Hilhorst, A. V. Petukhov, S. Bals, D. Vanmaekelbergh, *Science* 344 (2014) 1377.
- [24] D. Zhrebetskyy, M. Scheele, Y. Zhang, N. Bronstein, C. Thompson, D. Britt, M. Salmeron, P. Alivisatos, L. W. Wang, *Science* 344 (2014) 1380.
- [25] D. Li, M. H. Nielsen, J. R. Lee, C. Frandsen, J. F. Banfield, J. J. De Yoreo, *Science* 336 (2012) 1014.
- [26] D. D. Wanger, R. E. Correa, E. A. Dauler, M. G. Bawendi, *Nano Letters* 13 (2013) 5907.
- [27] D. M. Balazs, M. I. Nugraha, S. Z. Bisri, M. Sytnyk, W. Heiss, M. A. Loi, *Applied Physics Letters* 104 (2014) 112104.
- [28] M. J. Speirs, D. M. Balazs, H. H. Fang, L. H. Lai, L. Protesescu, M. V. Kovalenko, M. A. Loi, *J.Mater.Chem.A* 3 (2015) 1450.
- [29] Simon M. Sze, K. K. Ng, *Physics of Semiconductor Devices* (2007), Wiley-Interscience, Hoboken, N.J. .
- [30] P. T. Erslev, H. Chen, J. Gao, M. C. Beard, A. J. Frank, J. van de Lagemaat, J. C. Johnson, J. M. Luther, *Physical Review B* 86 (2012) 155313.
- [31] S. Z. Bisri, C. Piliego, M. Yarema, W. Heiss, M. A. Loi, *Advanced Materials* 25 (2013) 4309.
- [32] H. You, W. Wang, S. Yang, *ACS Applied Materials & Interfaces* 6 (2014) 19035.
- [33] H. Fang, R. Raissa, M. Abdu-Aguye, S. Adjokatse, G. R. Blake, J. Even, M. A. Loi, *Advanced Functional Materials* 25 (2015) 2378.
- [34] C. Piliego, L. Protesescu, S. Z. Bisri, M. V. Kovalenko, M. A. Loi, *Energy & Environmental Science* 6 (2013) 3054.
- [35] M. I. Nugraha, R. Häusermann, S. Z. Bisri, H. Matsui, M. Sytnyk, W. Heiss, J. Takeya, M. A. Loi, *Advanced Materials* 27 (2015) 2107.
- [36] M. S. Kang, A. Sahu, D. J. Norris, C. D. Frisbie, *Nano Letters* 11 (2011) 3887.

